Electrojet estimates from mesospheric magnetic field measurements

K. M. Laundal[1], J. H. Yee[2], V. G. Merkin[2], J. W. Gjerloev[1,2], H. Vanhamäki[3], J. P. Reistad[1], M. Madelaire[1], K. Sorathia[2]

[1]Birkeland Centre for Space Science, University in Bergen, Norway
[2]Applied Physics Laboratory, Johns Hopkins University, Laurel, MD 20723, USA
[3]Ionospheric Physics Research Unit, University of Oulu, Finland.

Key Points:

- We describe a technique to image the electrojet from low Earth orbit using the Zeeman effect
- Simulation results show that the technique can resolve fine-scale structures in the electrojet
- A novel inversion scheme for spherical elementary current representation is presented

Corresponding author: Karl Laundal, karl.laundal@uib.no

Abstract

The auroral electrojet is traditionally measured remotely with magnetometers on ground or in low Earth orbit (LEO). The sparse distribution of measurements, combined with a vertical distance of some 100 km to ground and typically >300 km to LEO satellites, means that smaller scale sizes can not be detected. Because of this, our understanding of the spatiotemporal characteristics of the electrojet is incomplete. Recent advances in measurement technology give hope of overcoming these limitations by multi-point remote detections of the magnetic field in the mesosphere, very close to the electrojet. We present a prediction of the magnitude of these disturbances, inferred from the spatiotemporal characteristics of magnetic field-aligned currents. We also discuss how a small satellite that carries Zeeman magnetic field sensors (Yee et al., 2020) could be used to essentially image the equivalent current at unprecedented spatial resolution. The electrojet imaging is demonstrated by combining carefully simulated measurements with a spherical elementary current representation using a novel inversion scheme.

Plain Language Summary

The interaction between the solar wind and the Earth's magnetic field produces electric currents in the ionosphere which are closely associated with auroral activity. The magnetic effects of these currents have so far been measured remotely, with ground magnetometers which are about 100 km below the currents, or with satellite magnetometers that are even further away, but above the currents. Since the currents have only been measured from a distance, we only know their large-scale structure. This limitation can be overcome by using new sensor technology that can be carried on small satellites in low Earth orbit. Such an instrument would measure oxygen emissions from the upper atmosphere, just below the currents. These emissions change in the presence of a magnetic field due to quantum effects, and can therefore be used to infer magnetic disturbances. We demonstrate a technique to create high-resolution 2D maps of the magnetic field disturbances, using simulated data from a proposed satellite mission.

1 Introduction

The first attempts to relate ground magnetic disturbances to electric currents in space were carried out more than a century ago. Birkeland (1908) presented a horizontal two-cell equivalent current system which is reminiscent of maps derived from modern magnetometer networks (Waters et al., 2015). Birkeland further proposed a 3D structure of the space currents that involved magnetic field-aligned currents. This idea remained controversial until it was confirmed by early magnetometer measurements in space (Zmuda et al., 1966). We now view the 3D ionospheric current system as composed of Birkeland currents, that flow along magnetic field lines, and a horizontal current that is confined to a thin conducting layer of the ionosphere, mainly around $100-120$ km altitude. The relationship between ground magnetic field observations and this 3D current system is ambiguous, and we therefore often interpret ground magnetic field observations in terms of an equivalent 2D current system. At high latitudes, the equivalent current is nearly identical with the divergence-free part of the horizontal current (e.g., Untiedt & Baumjohann, 1993; Fukushima, 1976). In this paper, we use the term electrojet as synonymous with the equivalent current, although it is some times used to refer to specific parts of it.

These days, it can be argued that the spatiotemporal structure of Birkeland currents is better known than the electrojet. Since the Birkeland current magnetic fields are measured *in-situ* with high-frequency satellite magnetometers, spatial structures as small as ~ 1 km can be investigated (Neubert & Christiansen, 2003). On the other hand, the electrojet magnetic field is measured at least ~ 100 km below the currents using ground magnetometers, or even further away above the currents using satellites (Olsen, 1996;

Laundal et al., 2016). Due to the large distance between the current and measurements, the small-scale structures of the electrojet is unknown. Measurements of the magnetic field at high altitudes, close to the horizontal ionospheric currents, would therefore provide new insight into structure and evolution of the electrojet system. Magnetic field measurements from the upper atmosphere would also represent an electrojet measurement with less contribution from ground induced currents (Juusola et al., 2020).

There are ongoing efforts to develop measurement techniques that would allow for regular sampling of the magnetic field closer to the ionospheric currents. Kane et al. (2018) demonstrated a technique to measure the magnetic field at about 100 km using a high-power pulsed laser beam to polarize mesospheric sodium, and a telescope to detect backscattered light. By changing the laser pulse frequency, a resonant frequency was detected which matches the Larmor frequency. The magnetic field was inferred from the Larmor frequency. The technique currently requires integration times that are longer than typical variations in the polar electrojet, and further development would therefore be needed to become truly useful for investigating small-scale variations in the current. Such efforts are underway by several groups.

Another approach was demonstrated by Yee et al. (2017). They used the Microwave Limb Sounder (MLS) on the Aura spacecraft to infer magnetic field disturbances based on the Zeeman effect. The MLS measures radiance spectra from the O_2 118 GHz line in order to infer atmospheric properties. However, the emissions are strongly affected by the Zeeman effect, which creates a split in the emission line that depends on the ambient magnetic field. Yee et al. (2017) showed that magnetic fields could be retrieved from these microwave spectra, and that variations in the magnetic field are in agreement with well-known electrojet properties.

Yee et al. (2017) also discussed how future more compact instruments for Zeeman magnetic field sensing could give new insight into the spatiotemporal behavior of the electrojet. Yee et al. (2020) presented a new conceptual instrument design that could be miniaturized and placed on a CubeSat. Such an instrument is proposed to fly on the Electrojet Zeeman Imaging Explorer (EZIE), which has been selected by NASA for concept studies. In this paper, we use simulated data from the EZIE mission, with a realistic ionospheric current system, main magnetic field, and instrument response, to show how it could be used to essentially image the electrojet and associated magnetic field.

In Section 1.1 we give a more quantitative description of the electrojet magnetic field on different heights. In Section 2 we describe the EZIE satellite mission and a novel technique to utilize such measurements to image the electrojet. We demonstrate the technique's feasibility using simulated data. In Section 3 we discuss potential improvements, challenges, and implications of the technique. Section 4 concludes the paper.

1.1 Electrojet magnetic field radial dependence

Since the mesosphere is resistive and presumably free of electric current, it is expected that magnetic disturbances there are associated with the same part of the ionospheric electric current system as is observed from ground. The variation in magnetic field strength as function of distance from the electrojet depends on scale size; large-scale currents are seen at greater distances than small-scale currents (e.g., Pulkkinen et al., 2006). Mesospheric magnetic field measurements will therefore enable us to resolve smaller spatial scales than what can be achieved with ground measurements. The purpose of this section is to quantify the height variation of the magnetic field disturbances, based on what we already know about the spatial structure of ionospheric currents.

The key assumption that we use is that the spatial power spectrum of the electrojet is proportional with the spatial power spectrum of the field-aligned electric currents (FACs). In contrast to the electrojet power spectrum, empirical estimates of the FAC

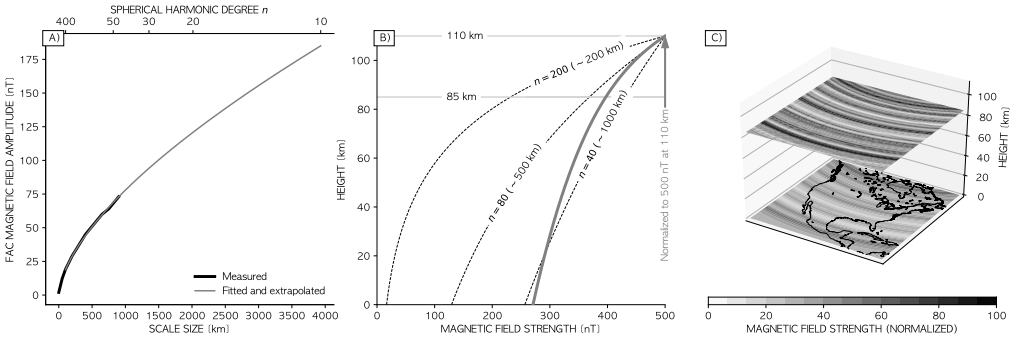

Figure 1. A) Average magnitude of the magnetic field disturbances associated with FACs as function of scale-size. The bold curve represents estimates by Gjerloev et al. (2011) based on data from the ST-5 mission. The gray curve is an extrapolation to larger scale-sizes based on a linear fit in log-log space. B) Bold gray: Altitude variation of the magnetic field associated with an electrojet whose spatial structure is given by the gray curve in panel A. Dashed: Altitude variation of magnetic field associated with equivalent current of certain scale sizes, as determined by spherical harmonic degree n. Each curve is normalized so that the magnetic field perturbation is 500 nT at 110 km. C) Contour plots of magnetic field of an electrojet whose spatial structure is given by the gray curve in panel A but is otherwise random. The magnetic field is shown at 85 km and on ground, and a map of North America is provided for scale.

spatial power spectrum are available. Figure 1A shows the spatial power spectrum of the magnetic field associated with FACs in bold black, from Gjerloev et al. (2011). The spectrum is based on magnetic field measurements from the three ST-5 satellites, which flew in a pearl-on-a-string configuration in polar low Earth orbit. Since this orbit intersects the FACs, the determination of small spatial scales is not restricted by distance, as for the electrojet. This particular spatial power spectrum is valid for the nightside during disturbed conditions (AL index < -100 nT). The spectrum is close to linear on a log-log scale, and we use this property to extrapolate to scale sizes which are longer than those considered by Gjerloev et al. (2011). The fitted and extrapolated curve is shown in gray.

The curves in Figure 1A, which represents the average magnitude of FAC magnetic field disturbances as function of scale size, is now assumed to also describe the spatial scale of the electrojet at zero distance from the current sheet. With this assumption, we can derive the radial variation of the magnetic field using results from spherical harmonic analysis. Equation 118 of Sabaka et al. (2010) describes the squared magnetic field, averaged over a sphere at radius $r \leq R$, where R is the current sheet radius, as

$$\langle \mathbf{B}(r)^2 \rangle = \sum_{n=1}^{\infty} n \left(\frac{r}{a}\right)^{2n-2} \sum_{m=0}^{n} [(q_n^m)^2 + (s_n^m)^2] = \sum_{n=1}^{\infty} n \left(\frac{r}{a}\right)^{2n-2} A_n. \quad (1)$$

n and m are spherical harmonic degree and order, respectively; $a = 6371.2$ km is a reference radius; and q_n^m and s_n^m are spherical harmonic coefficients. On the right hand side, the sum over spherical harmonic order m is written as A_n. The terms in the sum represent the extent to which each degree n contributes to the squared magnitude of the magnetic field.

The two x axes of Figure 1A represent scale size L (bottom) and spherical harmonic degree n (top). They are related by assuming that the scale size is equal to the meridional wavelength λ of the spherical harmonics, which is related to wavenumber n by Jean's

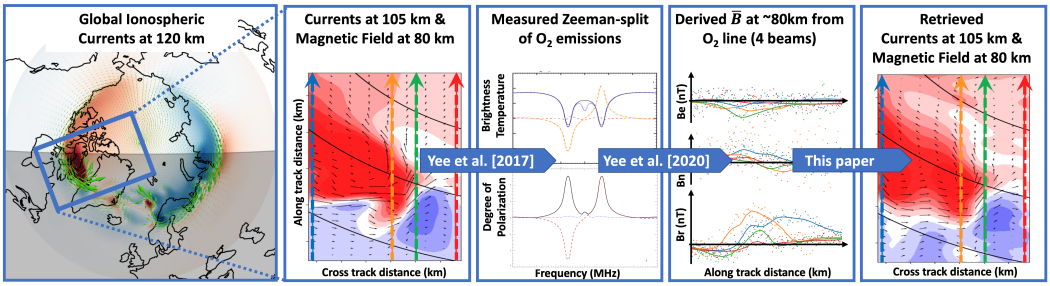

Figure 2. An illustrated outline of this paper: A high-resolution MHD simulation snapshot (left, described by Sorathia et al. (2020) and in Section 2.1) of the radial magnetic field at 80 km (color contours) and horizontal ionospheric current densities (green vectors). The MHD simulation is used to calculate realistic magnetic field perturbations in the field-of-view covered by an EZIE satellite during a 4 min time window (second panel). These perturbations are used to simulate the Zeeman split of the 118 GHz O_2, originating from the mesosphere at about 80 km (third panel, described by Yee et al. (2020)). The emissions are then used to produce realistic estimates of the magnetic field disturbance measurements, including noise (fourth panel, described in Section 2.2). This is described in Yee et al. (2020) and in Section 2.2. Finally, the simulated measurements shown at bottom right are used to estimate 2D maps of the electrojet and associated magnetic field (right panel, described in Section 2.3). The last step is the main focus of this paper.

formula $n = \frac{2\pi R_{FAC}}{\lambda} - \frac{1}{2}$. R_{FAC} is the radius at which the FAC power spectrum was evaluated by Gjerloev et al. (2011), 200 km altitude. This relationship allows us to find an estimate for A_n in equation (1), and thus calculate the average magnetic field magnitude at other radii using the same equation. The result is shown as a gray line in Figure 1B. This curve can be interpreted as a prediction of how the electrojet magnetic field decreases with distance, assuming that the electrojet has a similar spatial structure as FACs, and that ground induced current contributions are negligible. The dashed lines show the altitude variation of the magnetic field associated with an electrojet of specific scale sizes, calculated by evaluating the terms in equation (1) for $n = 40, 80$, and 200. These wavenumbers correspond to scale sizes of approximately 1000 km, 500 km, and 200 km, respectively. All curves in Figure 1B are normalized so that their magnitudes are 500 nT at 110 km. It is clear from this figure that only the large-scale features of the auroral electrojet are distinguishable from ground magnetometer measurements, and that more detail could be resolved with magnetic field measurements from mesospheric altitudes.

To further visualize the difference in the magnetic field structure at 85 km and on ground, we show in Figure 1C contour plots for a random electrojet whose spatial structure is given by the gray line in Figure 1A. The random magnetic field is constructed by assigning random spherical harmonic coefficients q_n^0 and s_n^0 which obey $(q_n^0)^2 + (s_n^0)^2 = A_n$. Longitudinal variations ($m > 0$) are ignored. The figure is not meant to show a realistic magnetic field, but rather to visualize the difference in spatial structure in the magnetic field disturbances at ground and in the mesosphere.

2 Estimating the electrojet from simulated mesospheric magnetic field measurements

EZIE was proposed to NASA as a Heliophysics Mission of Opportunity and is selected for concept studies. It consists of three satellites in low Earth orbit, equipped with four Zeeman magnetic field sensors each. These sensors will point towards the mesosphere separated in the cross-track direction, and thus observe emissions along four tracks as the satellite passes. We have used high-resolution magnetohydrodynamic (MHD) simulations to produce a realistic distribution of ionospheric currents and associated magnetic field disturbances, and modeled observations of mesospheric O_2 microwave spectra, including realistic measurement noise, with instruments mounted on a satellite in low Earth orbit. We have then used these synthetic observations to estimate maps of the auroral electrojet via two inversions: First to retrieve the magnetic disturbance field from the data, and then to calculate the equivalent current. The EZIE mission concept and the end-to-end simulation outline here are illustrated in Figure 2.

We describe the details of the MHD simulations in the next section. Then we describe how the simulated data were modeled, and how the magnetic field was retrieved from the observed Zeeman split. Finally we describe the details of the inversion to calculate equivalent currents and 2D-maps of the magnetic field vector components from the simulated measurements.

2.1 MHD simulation

The electric currents and magnetic field disturbances used in this study are taken from a snapshot of a global magnetosphere simulation published recently by Sorathia et al. (2020). This simulation of a synthetic substorm used the Grid Agnostic Magnetohydrodynamics with Extended Research Applications (GAMERA) code (Zhang et al., 2019) at an unprecedentedly high spatial resolution approaching the ion kinetic scales in the central plasma sheet and ∼30 km in the auroral ionosphere. While the original simulation by Sorathia et al. (2020) used a uniform Pedersen ionospheric conductance, for the numerical experiment presented here, we used the same field-aligned currents but replaced the conductance with the full auroral model (Fedder et al., 1995) to produce a realistic distribution of both Pedersen and Hall conductances. Using this conductance model, the standard ionospheric potential solution was obtained using a version of the Magnetosphere-Ionosphere Coupler/Solver (MIX) code (Merkin & Lyon, 2010) rewritten for GAMERA (dubbed REMIX). Thus, the distribution of the horizontal ionospheric currents was derived. In combination with the field-aligned currents, it was then used to derive the magnetic perturbation vectors at the EZIE measurement altitude using the Biot-Savart integration (Rastätter et al., 2014).

The magnetic field perturbations from the MHD simulation are used as input to model the sensor response and magnetic field retrieval to give a realistic set of measurements, described in Section 2.2. In Section 2.3 we use these simulated measurements to estimate the corresponding electrojet, and compare the estimated electrojet to the original MHD simulation. The MHD simulation electrojet is calculated by extracting the divergence-free part the ionospheric currents $\boldsymbol{j}_{df}$. This is achieved by use of Helmholtz' theorem which implies that $\boldsymbol{j}_{df} = \boldsymbol{j} - \boldsymbol{j}_{cf}$. The ionospheric horizontal current $\boldsymbol{j}$ and the field-aligned current $j_\parallel$ of the MHD simulation are well defined everywhere, and the curl-free part $\boldsymbol{j}_{cf}$ can be calculated from $\boldsymbol{j}_{cf} = \nabla\Psi$ where Ψ is the solution to $\nabla^2\Psi = -j_\parallel$ (e.g., Laundal et al., 2015).

2.2 Magnetic field inversion

Each of the three EZIE satellites is proposed to carry four sensors each allowing the determination of the mesospheric magnetic field via the Zeeman effect. The measure-

ment concept builds on the Microwave Limb Sounder on the Aura satellite (Waters et al., 2006), which measures radiance spectra from the atmospheric limb. Yee et al. (2017) showed that MLS spectra near the 118 GHz O_2 line could be used to retrieve the magnetic field in the mesosphere where the emissions originate. The EZIE sensors, which were described by Yee et al. (2020), differ from the MLS in that they are far more compact, weigh less, and require less power. Instead of pointing at the limb they observe in a near nadir direction, providing vastly improved geo-location of the emissions and thus the magnetic field measurement. In this paper, we use simulated measurements from the four sensors on-board a single satellite to retrieve the auroral electrojet in the region scanned by the satellite.

The simulated measurements represent a realistic instrument response to radiation near the 118 GHz microwave emissions from mesospheric O_2. The radiation, including the Zeeman effect, is modeled using the Atmospheric Radiative Transfer Simulator (based on formulations by Larsson et al. (2014)) with an MSIS atmosphere, and a realistic magnetic field model (Thébault et al., 2015) as a background for the GAMERA disturbances described in Section 2.1. The viewing geometries correspond to sensors mounted on a sun-synchronous satellite at 500 km, and pointing at fixed angles in the cross-track direction. The disturbance magnetic field components are simultaneously and iteratively retrieved along with their error covariances from the four measured Stokes vectors and their estimated uncertainties.

The EZIE measurement concept would give one magnetic field measurement per sensor every 2 seconds. With four simultaneous measurements for each satellite, we get measurements along four tracks in a push-broom configuration. The colored lines in the top panel of Figure 3 shows the paths formed by the measurement points in a four minute interval as the simulated satellite crosses the auroral zone. The lower panels in Figure 3 show the magnetic field components along each track, estimated from simulated microwave emissions. The colors correspond to the trajectory of the same color in the top plot. The solid lines show the magnetic field according to the MHD simulation, and the dots show the realistic simulated measurements including noise and other complicating effects. Notice that the vertical (nearly magnetic field-aligned) component is much more precisely determined than the two horizontal components. This is due to the viewing geometry with respect to the orientation of the magnetic field (Yee et al., 2020).

2.3 Electrojet inversion

Here we describe a procedure to use the measurements of the previous section to estimate a continuous map of the disturbance magnetic field and associated equivalent current in the region spanned by the Zeeman magnetic field sensors as the satellite traverses. To estimate a continuous map of the magnetic field and equivalent current, we use a divergence-free spherical elementary current representation. The spherical elementary current system (SECS) technique was developed by Amm (1997), and has since been widely used to estimate ionospheric currents from magnetic field measurements on ground and in space (Amm et al., 2015). The key idea is to model the ionospheric current as the sum of contributions from a set of basis functions that are centered at nodes strategically placed on a spherical shell at an ionospheric radius R_I. In our case, the nodes are placed at the center of the grid cells shown in Figure 3. Each basis function describes a horizontal surface current that circulates the node.

The magnetic field at location $\boldsymbol{r}$ can then be modeled as the combined effect of a set of K divergence-free elementary currents. A Biot-Savart integral over these surface currents is expressed as

$$\boldsymbol{B}(\boldsymbol{r}) = \frac{\mu_0}{4\pi} \int_S \frac{\left[\sum_{j=1}^{K} \frac{S_j}{4\pi R_I} \cot\left(\frac{\theta_{\boldsymbol{r}'\boldsymbol{r}_j}}{2}\right) \hat{\boldsymbol{\phi}}_j\right] \times \hat{\boldsymbol{r}}'}{\|\boldsymbol{r} - \boldsymbol{r}'\|^2} dS \tag{2}$$

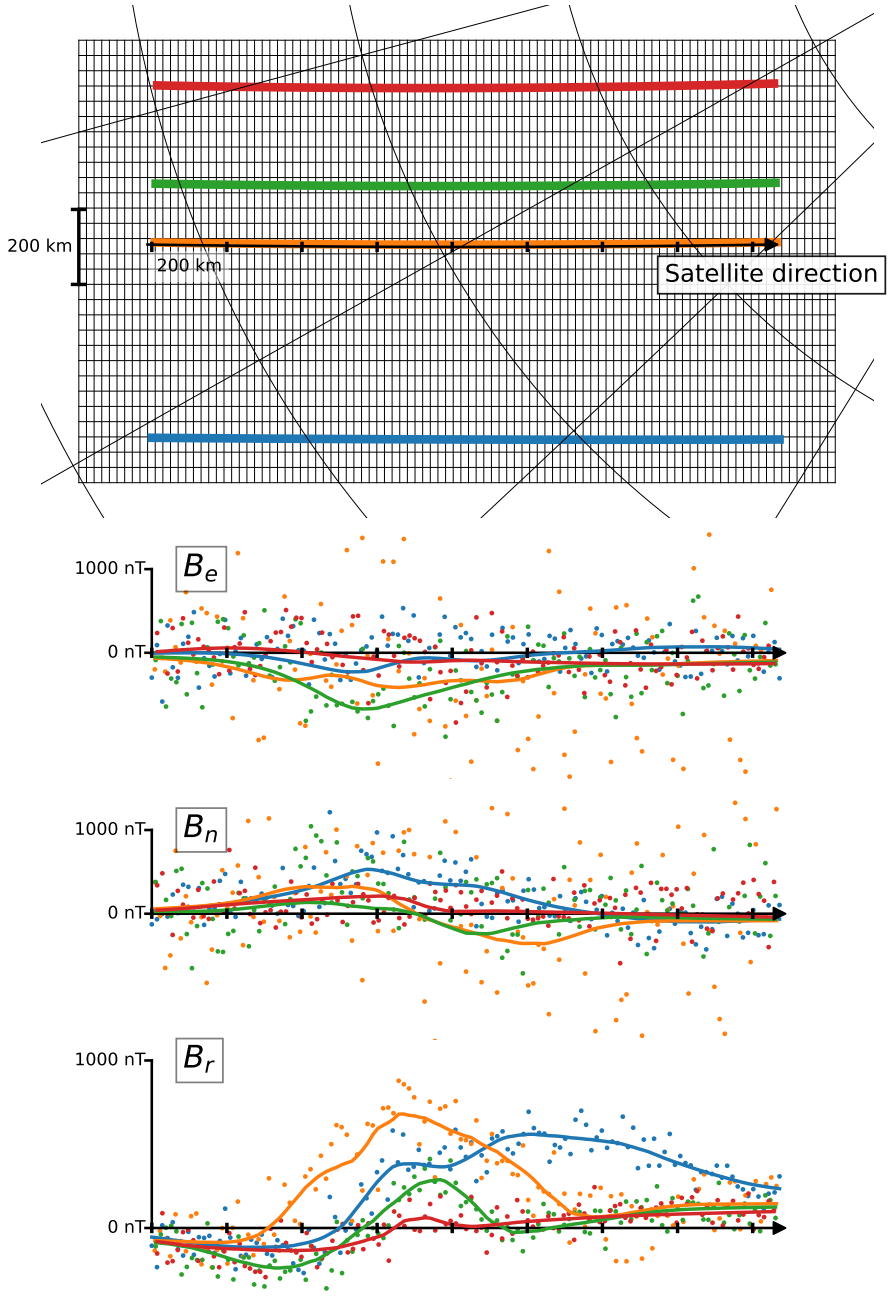

Figure 3. Top: SECS grid (black mesh) and measurement locations (colors) for a 4-min segment of simulated EZIE measurements. The spherical coordinate grid represents geomagnetic latitude and longitude. Bottom: The three components of the magnetic field retrieved from the simulated observed microwave spectra (dots) and the magnetic field according the MHD simulation (solid lines). The colors correspond to the trajectory of the same color in the top plot. The x axis is common among all plots, and the space between tick marks is 200 km. Notice the different scales of the y axes in the horizontal and radial components.

where primes denote the variable of integration ($\boldsymbol{r}'$), and the integral is over the entire spherical shell at $r = R_I$. The expression in square brackets is the divergence-free surface current density, and the summation index refers to the node at the center of each grid cell in Fig. 3. The nodes have amplitudes S_j and are located at $\boldsymbol{r}_j$. $\theta_{\boldsymbol{r}'\boldsymbol{r}_j}$ is the angle between $\boldsymbol{r}_j$ and $\boldsymbol{r}'$, and $\hat{\boldsymbol{\phi}}_j$ is a unit vector in the eastward direction in a coordinate system whose north pole is at $\boldsymbol{r}_j$. Amm & Viljanen (1999) presented a closed-form solution to the integral which does not depend on primed variables, which is what we use here. See also the review paper by Vanhamaki & Juusola (2020) for a more detailed overview of the technique and for the full set of relevant equations.

Given a set of K node locations ($\boldsymbol{r}_j$ in equation 2), the amplitudes S_j of each divergence-free current basis function can be estimated from a set of N magnetic field component measurements by solving an $N \times K$ set of linear equations. However, our measurements are non-uniformly distributed and fewer than the number of nodes. The solution to the under-determined set of equations is therefore highly dependent on the choice of grid (node locations), and on the way that the inverse problem is regularized (Vanhamaki & Juusola, 2020). When applying the SECS technique to EZIE data, it is critical that the grid and regularization technique are selected such that variations reflect geophysical changes and not changes in geometry, for example as the satellite moves.

We solve this problem by choosing a grid of nodes that changes minimally relative to the measurements as the satellite moves. We use a grid which is regular in a cubed sphere projection (Ronchi et al., 1996). This projection maps points on the sphere to a circumscribed cube. We only need to project to one of the sides of the cube since we focus on a relatively small region. We center this side on the satellite location at the time in the middle of the measurement segment, and align it with the satellite velocity vector. The grid, satellite track, measurement tracks, and geomagnetic coordinate contours are all shown in this projection at the top of Figure 3. Notice that the grid extends beyond the measurement tracks. The purpose of this is not to extrapolate, but to allow the exterior nodes to represent a uniform background current density (Vanhamaki & Juusola, 2020).

The SECS current amplitudes, $m = [S_1, S_2, \ldots, S_K]^\top$, are solutions to the set of equations

$$d = Gm \tag{3}$$

where d is a column vector of measured magnetic field components and G is the design matrix relating the magnetic field components and the DF SECS amplitudes according to equation 2. In this case, since all three magnetic field components are the result of an inversion from the same spectrum, the errors are correlated. That means that the effective number of equations in (3) is less than the number of elements in d. The system of equations can in principle be solved for m by generalized least squares (e.g., Riley et al., 2006, Chapter 31) by minimizing

$$f_0 = (d - Gm)^\top V^{-1}(d - Gm), \tag{4}$$

where V is the data covariance matrix, which contains off-diagonal terms due to the correlated errors. V is known from the magnetic field inversion.

However, the inverse problem is under-determined since the density of SECS poles is higher than the density of measurements almost everywhere. Therefore, additional information must be provided to yield physically meaningful solutions. We choose to add two terms to the cost function (4), to minimize the norm of the amplitude vector (L_2 regularization), and the gradient of SECS poles along magnetic circles of latitude. The total cost function is

$$f = f_0 + \lambda_1 \|Im\|_2 + \lambda_2 \|L_e m\|_2, \tag{5}$$

where λ_1 and λ_2 are damping parameters, I is the $K \times K$ identity matrix, and $\| \cdot \|_2$ indicates the Euclidean norm. L_e is a matrix that, when multiplied by m gives an es-

timate of the gradient of the SECS amplitudes in the magnetic eastward direction. We choose to penalize solutions that show variations in the magnetic longitudinal direction knowing that the electrojet tends to be extended in the longitudinal direction or in other words gradients in magnetic latitude typically exceed those in magnetic longitude.

In our implementation, the longitudinal gradient estimates are based on a first-order central difference scheme. Our choice of a regular grid of SECS poles in cubed sphere projected coordinates, together with the equations provided by Ronchi et al. (1996), greatly simplifies the calculation of L_e. The grid resolution is to some extent linked to the gradient evaluation, since the difference scheme accuracy increases with grid density. The number of nodes may thus potentially be reduced by increasing the order of the difference scheme. The need for a regular grid ostensibly removes one of the advantages of using the SECS representation: That pole density can be adjusted according to data density. However, variations in data density could be taken into account via regularization, by damping variations more strongly in regions with sparse data. We forgo this option here for simplicity.

The solution m that minimizes the cost function (5) can be written as

$$m = (G^\top V^{-1} G + \lambda_1 I + \lambda_2 L_e^\top L_e)^{-1} (G^\top V^{-1} d). \tag{6}$$

This way of solving the under-determined problem is different from the approach traditionally taken in SECS analysis, which is to ensure a smooth solution by truncated singular value decomposition. In our scheme, the damping parameter λ_1 plays the role of the singular value truncation level in traditional SECS analysis.

2.3.1 Results

Figure 4 shows six views of the region covered by the interior part of the grid in Figure 3. The grid is rotated 90°, and the satellite tracks are shown in the right column with similar color as in Fig. 3. The left column shows maps of the magnetic field perturbations of the MHD simulation at 80 km, with the component indicated in the top left corners. The gray vector field is the same in all six plots, and indicates the divergence-free part of the horizontal ionospheric current of the MHD simulation. The right column shows inversion results based on the data points shown in Fig 3, and the inversion scheme described above. The black vector field is the associated equivalent current.

Comparisons between inversion results and MHD simulation output show that the meso-scale features of the disturbance magnetic field are retrieved by the inversion. This is true for all three components despite the significant differences in noise between the components demonstrated in Figure 3. This is possible because the magnetic field components are not independent, but manifestations of the same electrojet. In our case, the radial component is most precisely measured, and therefore most important in the SECS inversion. Thus in principle, the relatively accurate measurement of the radial component can help increase the precision of the horizontal components via their relationship to an equivalent current.

Figure 4 shows that the match between MHD simulation and inversion result is better where the spacing between measurement tracks is small. The regularization technique ensures that interpolation between measurement tracks is mostly in the east-west direction. Nevertheless, prominent north-south structures are reproduced where dictated by the data. This is particularly evident in the bottom row, where there is a reversal in sign of B_r which is aligned in the north-south direction. The magnitude of the magnetic field and currents are well matched in regions with high data density, but expectedly underestimated due to damping elsewhere.

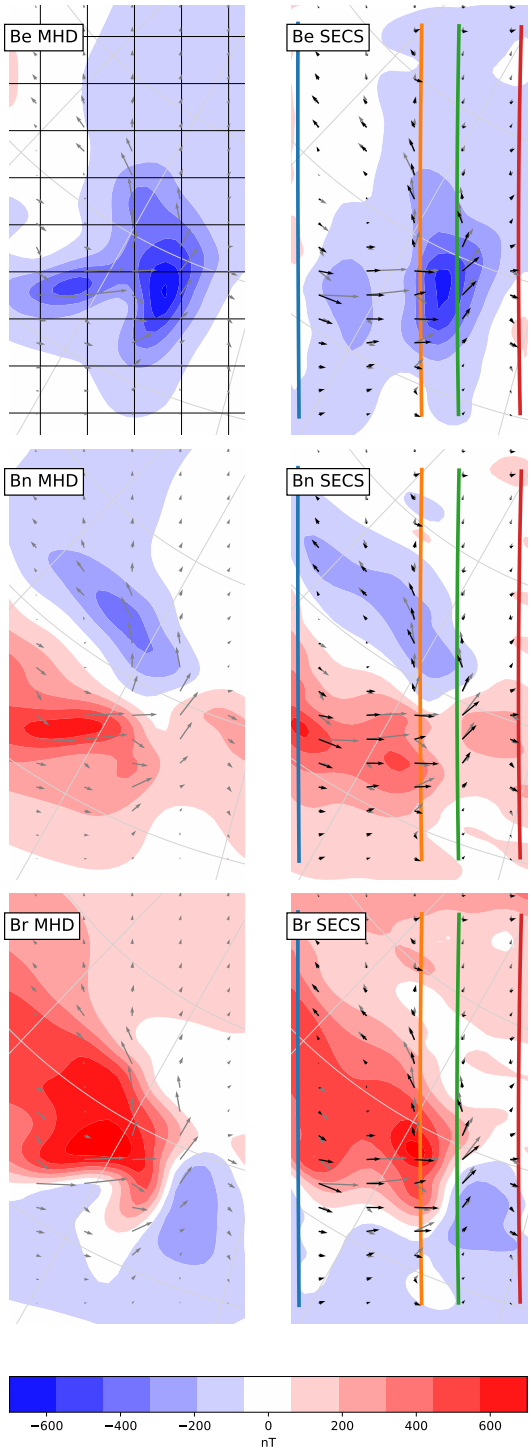

Figure 4. Comparisons between the MHD model output (left) and the SECS inversion results based on simulated EZIE measurements (right). Each column correspond to different magnetic field components. The divergence-free part of the MHD simulation ionospheric horizontal current is shown as gray arrows in all plots. Compare this to the divergence-free current of the inversion shown as black arrows in the right column. A 200 × 200 km grid is shown in the top left panel to indicate the scale sizes of the structures.

3 Discussion

We have shown how a low Earth orbiting satellite equipped with four sensors that observe the Zeeman split of mesospheric 118 GHz O_2 emissions can be used to produce 2D maps of the auroral electrojet. The background for this study is the demonstration of the measurement concept by Yee et al. (2017), the recent development of instrument technology (Yee et al., 2020), and the Electrojet Zeeman Imaging Explorer (EZIE) satellite mission which was selected by NASA for concept studies.

We have presented a novel technique to use spherical elementary current systems (SECS, Amm (1997)) to represent the electrojet which corresponds to simulated EZIE magnetic field measurements from 80 km altitude. The simulations involve high-resolution realistic background (Thébault et al., 2015) and perturbation (Sorathia et al., 2020) magnetic fields, and a realistic instrument response. The electrojet has so far been measured almost exclusively from distances of ∼100 km (ground based magnetometers) and with a network of sparse non-uniformly distributed stations that are fixed in the rotating Earth frame. These observational limitations can be overcome by a pearls-on-a-string mission such as EZIE. The good match between our SECS representation of the electrojet and the simulation shows that the measurement technique has the potential to fill this important knowledge gap.

3.1 Physical interpretation of the electrojet

As mentioned in the introduction, the equivalent current / electrojet is a theoretical horizontal sheet current whose magnetic perturbations are equivalent with the observed magnetic field perturbations under the ionosphere. Although the relationship to real 3D current systems is ambiguous, certain properties are helpful in the physical interpretation of equivalent currents: First of all, at high latitudes, where magnetic field lines are almost vertical, the equivalent current is nearly identical to the divergence-free part of the horizontal current. However, the divergence-free part of the horizontal current is also a rather abstract quantity, and it can be non-zero in regions which are current-free (e.g., Laundal et al., 2015). If we can assume that the electric field in the frame of the neutral wind is a potential field and parallel with conductance gradients, the equivalent current at high latitudes is equal to the Hall current. Furthermore, if the Hall/-Pedersen conductance ratio is constant, field-aligned currents are directly proportional to the curl of the equivalent current/electrojet (e.g., Amm et al., 2002). If these assumptions are violated, the relationship between the electrojet and the true 3D current system may be determined by combining with other measurements (auroral precipitation, ionospheric convection, field-aligned currents) (Richmond & Kamide, 1988).

Dependent on the science issue at hand, these subtleties may not be relevant. For example, present theories concerning the composition of the horizontal segment of the substorm current wedge are distinguishable by their predictions of a continuous versus structured horizontal current channel. Such differences would be directly reflected in the 2D equivalent current. In this case the main difference between the 2D equivalent current and the true 3D current would be their closure. Since the equivalent current by definition is horizontal, current channels that in reality connect to field-aligned currents will appear to close via large-scale horizontal return currents that enclose the channels (e.g., Laundal et al., 2018).

3.2 Effects of temporal variations

The electrojet retrieval presented here implicitly assumes that the current system remains static in the 4 min interval of the analysis. This assumption was automatically fulfilled, since the simulated magnetic field measurements are based on a single snapshot of magnetic field disturbances from an MHD simulation. However, as a mission such as

EZIE traverses the region of interest, the 2D inversion will include measurements that are separated in space as well as time. It will take the satellite around 2 min to traverse the auroral region. To determine to what extent the electrojet is static during this time we refer to the analysis presented by Gjerloev et al. (2011). They found that on the nightside features with scale sizes less than 250 km could on average be considered static over a 2 min period. They had no way of determining if a particular process took place (e.g. north-south streamers, polar boundary intensifications (PBIs) or other meso-scale features) but merely determined this scale size-variability relationship as an average over all conditions. We do, however, know both the scale size at ionospheric altitudes and the lifetime of several meso-scale features: PBIs (∼500 km / 8 min (e.g., Zou et al., 2014)); Streamers (∼350 km / 20 min (e.g., Sergeev et al., 2004)); and, Omega Bands (∼500 km/ 20 min (e.g., Partamies et al., 2017)). For a LEO satellite (∼8 km/s) it is thus questionable if PBIs can be considered static while streamers and omega bands may at first glance appear to fall into the static category. The concern, however, may be that for example streamers move which complicates the static assumption. This concern could potentially be checked if auroral imaging with sufficient spatial and temporal resolution as well as sufficiently large field-of-view was available. For a mission like EZIE these concerns imply that the science focus should be on processes with characteristics that suit the observational capabilities. A problem suitable for EZIE could be the structure and evolution of the substorm current wedge which is still being debated despite decades of studies. As a final note it should be mentioned that smaller scale sizes are typically more variable and should not be considered as static over the 2 min traversal time. However, as measurements are made some 30 km separated in altitude from the actual ionospheric currents these smaller scale sizes may not be captured anyway (see Figure 1).

3.3 Effects of volume emissions

The microwave spectrum observed with a Zeeman magnetic field sensor in low Earth orbit would represent a weighted average of the emissions in the sensor's field of view. Nevertheless, in the inversion presented above, each measurement was assigned the precise position of the center of the field of view. In this section we replace this precise value with a distribution, and investigate the corresponding distribution of solutions. The purpose of this is to give a rough estimate of how the fuzziness in measurement locations maps to a spread in the SECS magnetic field.

To do this, we apply the bootstrap method to the inversion described in Section 2.3: Instead of using the precise measurement locations, we draw random values according to probability distributions that mimic the EZIE field of view, and repeat the inversion many times. The EZIE sensors' field of view in the mesosphere would be around 40 km, and we define a corresponding probability distribution by sliding a 2D Gaussian with $\sigma = 10$ km along the measurement track by a distance of ≈ 15 km, corresponding to the 2 second integration time used in this study. A set of random samples from these distributions give a set of measurement locations, and a corresponding solution vector from equation (6). An example of the magnetic field of such a random dataset is shown in the second column of Figure 5, next to the inversion result based on an exact measurement location in the first column (a copy of the right column from Figure 4). The magnetic field structures are clearly very similar in the two columns.

The third column in Figure 5 shows the mean magnetic field of 30,000 randomly re-sampled datasets, and the fourth (rightmost) column shows the standard deviation. An analysis of the distributions of the model parameters S_j show that they converge after about 7,000 repetitions, which means that the statistics presented in these columns are reliable. We see that the difference between the mean magnetic field and the magnetic field in the left column is very small. The standard deviation is mostly in the order of ≈ 10 nT, but reaches ≈ 50 nT near the middle measurement track. This is approximately the magnitude of the error that we can expect in the predicted magnetic

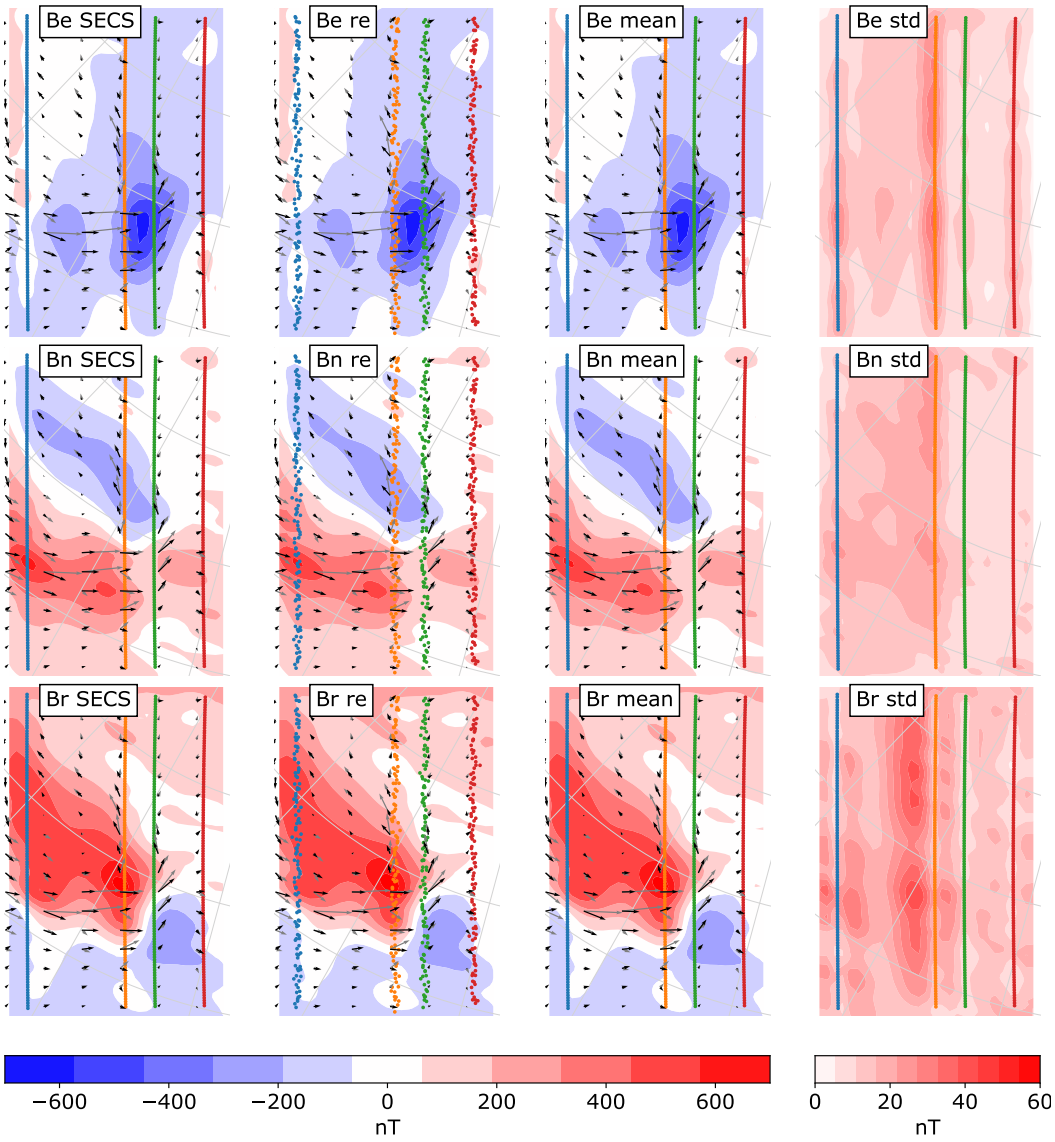

Figure 5. Results of a bootstrap experiment to investigate the effect of imprecise measurement locations. Each row corresponds to eastward, northward, and upward components of the magnetic field, respectively, while the columns correspond to (from left to right): 1) The magnetic field according to the method described in Section 2.3. This is identical to the right column of Figure 4, repeated here to help comparison with the other columns. 2) The magnetic field from one of the re-sampled datasets (notice scattered measurement locations). 3) The average magnetic field of all 30,000 re-sampled datasets. 4) The standard deviation of the magnetic field in all the datasets. The black vectors show the corresponding equivalent currents, while the gray vectors show the MHD simulation divergence-free horizontal current.

field due to uncertainties in measurement locations. The black arrows in Figure 5 represent the SECS equivalent current, and the gray arrows the MHD divergence-free current. The mean equivalent current vectors from the 30,000 re-sampled datasets are visually indistinguishable from the SECS currents based on precise measurement locations.

3.4 Possible improvements of the electrojet estimation

The electrojet estimation technique presented in Section 2.3 involves a novel approach for regularization of the SECS amplitude inversion. Our approach is arguably more flexible than the traditional method (Vanhamaki & Juusola, 2020), since it allows us to impose constraints other than a uniform spatial smoothing. In this paper we included a penalty for solutions that vary in the magnetic east-west direction, but we expect that there are additional ways in which knowledge about the physics of the electrojet could help inform the inversion.

One strategy could be to use knowledge about the ionospheric conductivity. We know that in the winter, magnetic field perturbations on ground (and hence in the mesosphere) are largely related to currents in the auroral zone (Laundal et al., 2015) where the conductivity is enhanced by ionizing particle precipitation. Knowledge about the location of the auroral oval would enable us to confine SECS amplitudes to this region. Simultaneous observations of the aurora could also be used to make a more precise determination of the preferred direction of variation; instead of penalizing variation in the magnetic east-west direction we could add a penalty for variations along the observed auroral arcs. A similar idea but different application and implementation was used in a recent study by Clayton et al. (2019).

It could also be beneficial to use knowledge about the magnetic field-aligned current (FAC) system in the inversion. As mentioned above, the divergence-free SECS amplitudes are proportional to field-aligned currents under certain conditions. Thus we expect that the SECS amplitudes and FACs are spatially correlated. Global FAC estimates are available from the AMPERE (Waters et al., 2020) project at 2 min cadence, based on 10 min of data from the fleet of Iridium satellites. EZIE would be able to provide spatial resolution far better than AMPERE but they could nevertheless help provide a baseline for the map of SECS amplitudes. It would also be straightforward to include ground magnetic field measurements in the electrojet estimates. This could improve the estimates of large-scale structures and mitigate boundary effects related to uniform electrojets that flow through the analysis area.

4 Conclusions

While the Zeeman magnetic field measurement technique is well established for sensing cosmic magnetic fields, it is new in the context of geospace. The primary benefits of such measurements are the close proximity between the detected magnetic field and the electric current, and the ability to remotely measure the magnetic field at multiple points simultaneously. The EZIE mission concept involves three satellites that scan the electrojet magnetic field as they pass over the auroral zone. In comparison to traditional techniques used for electrojet analyses, the measurement precision is poor, and even the source location is inexact. The electrojet inversion technique presented here uses statistics and knowledge about the nature of the electrojet to overcome these challenges.

Although the inversion scheme in Section 2.3 was developed with the EZIE satellite concept in mind, it would be straightforward to combine with data from ground magnetometers in the vicinity of the satellite. We also believe that the ideas behind the grid and inversion, including possible improvements described in Section 3.4, will be useful in other analyses of regional ionospheric electrodynamics. The technique could be ap-

plied with both ground and space magnetometers, or for estimating ionospheric convection using the The Super Dual Auroral Radar Network (e.g., Reistad et al., 2019).

Acknowledgments

K.M. Laundal, J.P. Reistad, and M. Madelaire are supported by the Research Council of Norway/CoE under contract 223252/F50 and the Trond Mohn Foundation. H. Vanhamäki was supported by Academy of Finland project 314664. V. G. Merkin and K. A. Sorathia acknowledge support from the NASA DRIVE Science Center for Geospace Storms (CGS) under Grant 80NSSC20K0601. The authors gratefully acknowledge the work done by the EZIE mission concept team in support of this paper.

The simulation dataset used in this study is available at https://doi.org/10.18710/8POYRY. Python code for working with spherical elementary current systems and cubed sphere coordinates is available at https://github.com/klaundal/secsy

References

Amm, O. (1997). Ionospheric elementary current systems in spherical coordinates and their application. *J. Geomag. Geoelectr.*, 947-955.

Amm, O., Engebretson, M. J., Hughes, T., Newitt, L., Viljanen, A., & Watermann, J. (2002). A traveling convection vortex event study: Instantaneous ionospheric equivalent currents, estimation of field-aligned currents, and the role of induced currents. *Journal of Geophysical Research: Space Physics*, *107*(A11), SIA 1-1-SIA 1-11. doi: 10.1029/2002JA009472

Amm, O., Vanhamäki, H., Kauristie, K., Stolle, C., Christiansen, F., Haagmans, R., ... Escoubet, C. P. (2015). A method to derive maps of ionospheric conductances, currents, and convection from the swarm multisatellite mission. *Journal of Geophysical Research: Space Physics*, *120*(4), 3263-3282. doi: 10.1002/2014JA020154

Amm, O., & Viljanen, A. (1999). Ionospheric disturbance magnetic field continuation from the ground to the ionosphere using spherical elementary current systems. *Earth Planets and Space*, 431-440. doi: 10.1186/BF03352247

Birkeland, K. R. (1908). *The norwegian aurora borealis expedition 1902-1903.* Christiania: H. Aschehoug & Co.

Clayton, R., Lynch, K., Zettergren, M., Burleigh, M., Conde, M., Grubbs, G., ... Varney, R. (2019). Two-dimensional maps of in situ ionospheric plasma flow data near auroral arcs using auroral imagery. *Journal of Geophysical Research: Space Physics*, *124*(4), 3036-3056. doi: 10.1029/2018JA026440

Fedder, J. A., Slinker, S. P., Lyon, J. G., & Elphinstone, R. D. (1995). Global numerical simulation of the growth phase and the expansion onset for a substorm observed by viking. *Journal of Geophysical Research: Space Physics*, *100*(A10), 19083-19093. doi: 10.1029/95JA01524

Fukushima, N. (1976). Generalized theorem for no ground magnetic effect of vertical currents connected with pedersen currents in the uniform-conductivity ionosphere. *Rep. Ionos.Space Res.Jap*, *30*, 35-50.

Gjerloev, J. W., Ohtani, S., Iijima, T., Anderson, B., Slavin, J., & Le, G. (2011). Characteristics of the terrestrial field-aligned current system. *Annales Geophysicae*, *29*(10), 1713–1729. doi: 10.5194/angeo-29-1713-2011

Juusola, L., Vanhamäki, H., Viljanen, A., & Smirnov, M. (2020). Induced telluric currents play a major role in the interpretation of geomagnetic variations. *Annales Geophysicae Discussions*, *2020*, 1–23. doi: 10.5194/angeo-2020-21

Kane, T. J., Hillman, P. D., Denman, C. A., Hart, M., Phillip Scott, R., Purucker, M. E., & Potashnik, S. J. (2018). Laser remote magnetometry using mesospheric sodium. *Journal of Geophysical Research: Space Physics*, *123*(8), 6171-6188. doi: 10.1029/2018JA025178

Larsson, R., Buehler, S. A., Eriksson, P., & Mendrok, J. (2014). A treatment of the zeeman effect using stokes formalism and its implementation in the atmospheric radiative transfer simulator (arts). *Journal of Quantitative Spectroscopy and Radiative Transfer*, *133*, 445 - 453. doi: https://doi.org/10.1016/j.jqsrt.2013.09.006

Laundal, K. M., Finlay, C. C., & Olsen, N. (2016). Sunlight effects on the 3D polar current system determined from low Earth orbit measurements. *Earth Planets Space*. doi: 10.1186/s40623-016-0518-x

Laundal, K. M., Finlay, C. C., Olsen, N., & Reistad, J. P. (2018). Solar wind and seasonal influence on ionospheric currents from Swarm and CHAMP measurements. *J. Geophys. Res.*. doi: 10.1029/2018JA025387

Laundal, K. M., Haaland, S. E., Lehtinen, N., Gjerloev, J. W., Ostgaard, N., Tenfjord, P., ... Anderson, B. J. (2015). Birkeland current effects on high-latitude ground magnetic field perturbations. *Geophys. Res. Lett.*. doi: 10.1002/2015GL065776

Merkin, V. G., & Lyon, J. G. (2010). Effects of the low-latitude ionospheric boundary condition on the global magnetosphere. *Journal of Geophysical Research: Space Physics*, *115*(A10). doi: 10.1029/2010JA015461

Neubert, T., & Christiansen, F. (2003). Small-scale, field-aligned currents at the top-side ionosphere. *Geophysical Research Letters*, *30*(19). doi: 10.1029/2003GL017808

Olsen, N. (1996). A new tool for determining ionospheric currents from magnetic satellite data. *Geophysical Research Letters*, *23*(24), 3635–3638. doi: 10.1029/96GL02896

Partamies, N., Weygand, J. M., & Juusola, L. (2017). Statistical study of auroral omega bands. *Annales Geophysicae*, *35*(5), 1069–1083. doi: 10.5194/angeo-35-1069-2017

Pulkkinen, A., Klimas, A., Vassiliadis, D., Uritsky, V., & Tanskanen, E. (2006). Spatiotemporal scaling properties of the ground geomagnetic field variations. *Journal of Geophysical Research: Space Physics*, *111*(A3). doi: 10.1029/2005JA011294

Rastätter, L., Tóth, G., Kuznetsova, M. M., & Pulkkinen, A. A. (2014). CalcDeltaB: An efficient postprocessing tool to calculate ground-level magnetic perturbations from global magnetosphere simulations. *Space Weather*, *12*(9), 553-565. doi: 10.1002/2014SW001083

Reistad, J. P., Laundal, K. M., Østgaard, N., Ohma, A., Haaland, S., Oksavik, K., & Milan, S. E. (2019). Separation and quantification of ionospheric convection sources: 1. A new technique. *J. Geophys. Res. - Space Physics*. doi: 10.1029/2019JA026634

Richmond, A. D., & Kamide, Y. (1988). Mapping electrodynamic features of the high-latitude ionosphere from localized observations: Technique. *J. Geophys. Res.*, *93*, 5741-5759. doi: 10.1029/JA093iA06p05741

Riley, K. F., Hobson, M. P., & Bence, S. J. (2006). *Mathematical methods for physics and engineering* (3rd ed.). Cambridge, UK: Cambridge University Press.

Ronchi, C., Iacono, R., & Paolucci, P. S. (1996). The "Cubed Sphere": A New Method for the Solution of Partial Differential Equations in Spherical Geometry. *Journal of Computational Physics*, *124*(1), 93 - 114. doi: 10.1006/jcph.1996.0047

Sabaka, T. J., Hulot, G., & Olsen, N. (2010). Handbook of geomathematics. In W. Freeden, M. Z. Nashed, & T. Sonar (Eds.), (pp. 503–538). Berlin, Heidelberg: Springer Berlin Heidelberg. doi: 10.1007/978-3-642-01546-5_17

Sergeev, V. A., Liou, K., Newell, P. T., Ohtani, S.-I., Hairston, M. R., & Rich, F. (2004). Auroral streamers: characteristics of associated precipitation,convection and field-aligned currents. *Annales Geophysicae*, *22*(2), 537–548. doi: 10.5194/angeo-22-537-2004

Sorathia, K. A., Merkin, V. G., Panov, E. V., Zhang, B., Lyon, J. G., Garretson, J., ... Wiltberger, M. (2020). Ballooning-interchange instability in the

near-Earth plasma sheet and auroral beads: Global magnetospheric modeling at the limit of the MHD approximation. *Geophysical Research Letters*. doi: 10.1029/2020GL088227

Thébault, E., Finlay, C., Beggan, C., Alken, P., Aubert, J., Barrois, O., ... Zvereva, T. (2015). International geomagnetic reference field: the 12th generation. *Earth, Planets and Space*, *67*. Retrieved from `http://dx.doi.org/10.1186/s40623-015-0228-9` doi: 10.1186/s40623-015-0228-9

Untiedt, J., & Baumjohann, W. (1993). Studies of polar current systems using the IMS Scandinavian magnetometer array. *Space Sci. Rev.*, 245-390.

Vanhamaki, H., & Juusola, L. (2020). Introduction to spherical elementary current systems. In *Ionospheric multi-spacecraft analysis tools* (pp. 5–33). ISSI Scientific Report Series 17. doi: 10.1007/978-3-030-26732-2_2

Waters, C. L., Anderson, B. J., Green, D. L., Korth, H., Barnes, R. J., & H. Vanhamäki, H. (2020). Science data products for ampere. In M. W. Dunlop & H. Lühr (Eds.), *Ionospheric multi-spacecraft analysis tools: Approaches for deriving ionospheric parameters* (pp. 141–165). Cham: Springer International Publishing. doi: 10.1007/978-3-030-26732-2_7

Waters, C. L., Gjerloev, J. W., Dupont, M., & Barnes, R. J. (2015). Global maps of ground magnetometer data. *Journal of Geophysical Research: Space Physics*, *120*(11), 9651-9660. doi: 10.1002/2015JA021596

Waters, J. W., Froidevaux, L., Harwood, R. S., Jarnot, R. F., Pickett, H. M., Read, W. G., ... Walch, M. J. (2006). The Earth observing system microwave limb sounder (EOS MLS) on the aura Satellite. *IEEE Transactions on Geoscience and Remote Sensing*, *44*(5), 1075-1092.

Yee, J. H., Gjerloev, J., Wu, D., & Schwartz, M. J. (2017). First Application of the Zeeman Technique to Remotely Measure Auroral Electrojet Intensity From Space. *Geophysical Research Letters*, *44*(20), 10,134-10,139. doi: 10.1002/2017GL074909

Yee, J. H., Gjerloev, J. W., & Wu, D. L. (2020). Remote Sensing of Magnetic Fields Induced by Electrojets From Space: Measurement Techniques and Sensor Design. In *Advances in Upper Atmosphere Research: Dynamics and Energetics.* AGU - in press.

Zhang, B., Sorathia, K. A., Lyon, J. G., Merkin, V. G., Garretson, J. S., & Wiltberger, M. (2019). GAMERA: A Three-dimensional Finite-volume MHD Solver for Non-orthogonal Curvilinear Geometries. *The Astrophysical Journal Supplement Series*, *244*(1). doi: 10.3847/1538-4365/ab3a4c

Zmuda, A. J., Martin, J. H., & Heuring, F. T. (1966). Transverse magnetic disturbances at 1100 kilometers in the auroral region. *Journal of Geophysical Research*, *71*(21), 5033–5045. doi: 10.1029/JZ071i021p05033

Zou, Y., Nishimura, Y., Lyons, L. R., Donovan, E. F., Ruohoniemi, J. M., Nishitani, N., & McWilliams, K. A. (2014). Statistical relationships between enhanced polar cap flows and PBIs. *Journal of Geophysical Research: Space Physics*, *119*(1), 151-162. doi: 10.1002/2013JA019269